Radiography in high mass X-ray binaries

Micro-structure of the stellar wind through variability of the column density

I. El Mellah[1], V. Grinberg[2], J. O. Sundqvist[3], F. A. Driessen[3], and M. A. Leutenegger[4]

[1] Centre for mathematical Plasma Astrophysics, Department of Mathematics, KU Leuven, Celestijnenlaan 200B, B-3001 Leuven, Belgium
e-mail: `ileyk.elmellah@kuleuven.be`
[2] Institut für Astronomie und Astrophysik, Universität Tübingen, Sand 1, 72076 Tübingen, Germany
[3] Institute of Astronomy, KU Leuven, Celestijnenlaan 200D, B-3001 Leuven, Belgium
[4] NASA Goddard Space Flight Center, 8800 Greenbelt Rd., Greenbelt, MD 20771, USA

ABSTRACT

Context. In high mass X-ray binaries, an accreting compact object orbits a high mass star which loses mass through a dense and inhomogeneous wind.
Aims. Using the compact object as an X-ray backlight, the time variability of the absorbing column density in the wind can be exploited in order to shed light on the micro-structure of the wind and obtain unbiased stellar mass loss rates for high mass stars.
Methods. We developed a simplified representation of the stellar wind where all the matter is gathered in spherical "clumps" radially advected away from the star. This model enables us to explore the connections between the stochastic properties of the wind and the variability of the column density for a comprehensive set of parameters related to the orbit and to the wind micro-structure, such as the size of the clumps and their individual mass. In particular, we focus on the evolution with the orbital phase of the standard deviation of the column density and of the characteristic duration of enhanced absorption episodes. Using the porosity length, we derive analytical predictions and compare them to the obtained standard deviations and coherence time scales.
Results. We identified the favorable systems and orbital phases to determine the wind micro-structure. The coherence time scale of the column density is shown to be the self-crossing time of a clump in front of the compact object. We thus provide a recipe to get accurate measurements of the size and of the mass of the clumps, purely based on the observable time variability of the column density.
Conclusions. The coherence time scale grants direct access to the size of the clumps while their mass can be deduced separately from the amplitude of the variability. If it is due to unaccreted passing-by clumps, the high column density variations in some high mass X-ray binaries would require high mass clumps to reproduce the observed peak-to-peak amplitude and coherence time scales. These clump properties are marginally compatible with the ones derived from radiative-hydrodynamics simulations. Alternatively, other components could contribute to the variability of the column density: larger orbital scale structures produced by a mechanism still to be identified, or a dense environment in the immediate vicinity of the accretor such as an accretion disk, an outflow or a spherical shell around the magnetosphere of the accreting neutron star.

Key words. accretion, accretion discs – X-rays: binaries – stars: black holes, neutron, supergiants, winds – methods: numerical

1. Introduction

Massive stars live a forceful life during which they shape galaxies with their mechanical, radiative and chemical feedback. Evolutionary pathways of massive stars are largely controlled by their line-driven winds, with typical mass loss rates $10^{-6} M_\odot \cdot \text{yr}^{-1}$ and terminal wind speeds of the order of $1\,000 \text{km} \cdot \text{s}^{-1}$ (Puls et al. 2008). The flow is provided with net outward momentum thanks to the resonant line absorption of UV stellar photons by partly ionized metal ions present in the outer envelope of the star. As the wind accelerates, it keeps tapping higher energy photons thanks to Doppler shift (Lucy & Solomon 1970; Castor et al. 1975).

Originally these line-driven winds were treated as smooth, steady-state outflows without any internal shocks or overdensity. However, it has been know for a long time now that they are in fact highly structured and variable on a broad range of spatial and temporal scales (for overviews, see Hamann et al. 2008; Sundqvist et al. 2012; Puls et al. 2015). Indeed, the de-

pendence of the acceleration on the velocity profile itself provokes the emergence of a self-growing feedback loop, the line-deshadowing instability, responsible for internal shocks and the formation of overdense regions or "clumps" (Owocki & Rybicki 1984; Owocki et al. 1988; Feldmeier 1995). This clumping can then severely affect the radiative transfer computations used to derive synthetic observables; as just one example, neglecting wind clumping leads to empirically inferred mass-loss rates that may differ by an order of magnitude for the same star, depending on which observational diagnostic is used to estimate the mass loss (Fullerton et al. 2006). Typically, mass-loss rates derived from diagnostics with opacities depending on the square of the density (for example the Hα line and thermal radio emission) are overestimated if clumping is neglected, whereas those derived from diagnostics depending linearly on density (usually UV resonance lines) can be underestimated if the light-leakage effects of a wind that is porous in velocity-space are not properly taken into account (e.g., Sundqvist & Puls 2018). X-ray emis-

sion line shapes from single stars offer an alternative mass-loss rate diagnostic based on continuum photoelectric opacity which is linear in density and insensitive to velocity field inhomogeneity (Owocki & Cohen 2001; Cohen et al. 2014). This diagnostic might still be compromised by geometrical porosity (Feldmeier et al. 2003; Sundqvist et al. 2012), although observational constraints disfavor the extreme degree of wind structure that would be needed for this (Leutenegger et al. 2013). Due to the faintness of X-ray emission from single stars and the modest size of existing X-ray telescopes, this diagnostic is currently limited to a handful of nearby objects.

High-mass X-ray binaries (HMXBs) can shed a unique light upon the mass loss and micro-structure of line-driven winds. In Supergiant X-ray binaries (SgXBs), a sub-class of HMXBs where a compact object, generally a neutron star (NS), sometimes a black hole (BH), orbits a blue supergiant and accretes part of its winds (Walter et al. 2015; Martínez-Núñez et al. 2017). The material captured heats up as it falls into the gravitational potential well and emits copious amounts of X-rays from the immediate vicinity of the compact object. Two methods have been proposed in order to use the X-ray point source as a probe and bring constrains on the wind clumpiness independent from the ones obtained with diagnostics for isolated massive star (Martínez-Núñez et al. 2017).

In the first method, if the episodic enhancements of the intrinsic X-ray luminosity observed in SgXBs are due to the direct capture of a clump, the amount of mass in a clump and the number of clumps per unit volume could be estimated (In't Zand 2005). This idea was applied both in persistent SgXBs (also called classic SgXBs, with low intrinsic variability) and in supergiant fast X-ray transients (SFXTs Bozzo et al. 2017). Oskinova et al. (2012) have calculated synthetic X-ray lightcurves that would result from this approach and compared the expected variability to the observed. This approach presupposes that the variability induced by the wind micro-structure remains unaltered from the orbital scale all the way down to the X-ray emitting region (either the NS surface or the inner rim of the accretion disk surrounding the BH). However, additional structures form, such as a hydrodynamics bow shock around the accretor, which have been shown to lower the variability compared to a purely ballistic model of the clump capture (El Mellah et al. 2018). The amount of material involved in a flare is thus an upper limit on the mass of a clump: a flare might be triggered by the capture of a clump but likely involves additional material which has been previously piling up at the outer rim of the NS magnetosphere due to the magneto-centrifugal gating mechanism (or propeller effect, Illarionov & Sunyaev 1975; Grebenev & Sunyaev 2007; Bozzo et al. 2008), in a quasi-spherical hot shell on top of the NS magnetosphere (Shakura et al. 2013) or in a disk-like structure (El Mellah et al. 2019b; Karino et al. 2019). Furthermore, Pradhan et al. (2018) concluded that the higher variability of the emission in SFXTs compared to SgXBs was likely due to mechanisms inhibiting accretion near the accretor, rather than clump capture. Also, Hainich et al. (2020) showed that there was no systematic difference between the stellar properties in classic SgXBs and in SFXTs. Since the stellar properties determine how inhomogeneous the wind is (Driessen et al. 2019), the intrinsic variability of the X-ray emission in HMXBs is likely a poor tracer of the micro-structure.

In a second method, one can make use of the highly variable absorption local to the HMXBs. If the variations in the absorbing column density are due to unaccreted clumps passing through the line-of-sight (LOS), the accretor could play the role of a steady backlight whose shimmering betrays the stochastic

properties of the wind it is embedded into (Oskinova et al. 2012; Grinberg et al. 2015). Time resolved spectroscopy enables us to monitor the absorbing column density directly (e.g. Haberl et al. 1989; Martínez-Núñez et al. 2014; Grinberg et al. 2015). Shorter timescales may be indirectly accessible via changes in X-ray color (e.g., Grinberg et al. 2017; Bozzo et al. 2017), especially when using multiple energy bands and working with color-color diagrams (Nowak et al. 2011; Hirsch et al. 2019). Grinberg et al. (2015) laid the foundations of a model of the clumps to relate the observed dips in the X-ray light curve of the HMXB Cygnus X-1 to the micro-structure of the wind. They assumed spherical clumps emitted by the donor star on radial trajectories. However, their exploration was driven by the measurements available using the particular set of observations discussed in their work and limited to the well known parameters of one particular system whose observable properties their model aimed to reproduce. In this paper, we expand on this first ansatz. We aim at designing a model suitable to grasp the complexity of the flow while still including analytically derivable predictions to prove its robustness. We want to determine whether, in realistic conditions, we can draw conclusions on the wind micro-structure in spite of the large number of clumps and of the diversity of clump properties along the LOS.

New insights have been provided on the clump properties thanks to multi-dimensional radiative hydrodynamics simulations by Sundqvist et al. (2018). The small size of the clumps deduced from first principles, of the order of 1% of the stellar radius at one stellar radius above the photosphere, is marginally compatible with observations, although it can differ depending on the stellar properties. On the other hand, Sander et al. (2017a) determined 1D steady radial velocity profiles of line-driven winds based on radiative transfer calculations in a steady-state hydrodynamic atmosphere in non-local thermodynamical equilibrium. It showed that the wind accelerates slower than previously thought, with dramatic consequences for the accretion process onto wind-fed compact objects in HMXBs (El Mellah et al. 2019b). Motivated by these new results, we want to focus on the impact of the clumps of the time variability of the column density profile compared to a smooth wind configuration. In this first approach, we discard other sources of variability such as larger scale structures produced by the orbital motion for instance. Based on a minimal representation of a clumpy wind, we study the connections of the wind micro-structure with the median value, the amplitude variations and the coherence time scales of the column density.

In section 2, we describe the ingredients of the model we developed and the numerical procedure we follow to compute the column density produced by clumps in number high enough to match the expected number of clumps around massive stars in HMXBs. In section 3, we present the analytic derivation of the column density variance that we confront to the numerical results in section 4, where we also report on the characteristic time scales of absorption episodes and the dependences with respect to the parameters of the model. In section 5, we present how these results can be used to constrain the wind micro-structure from observations, while the limitations of our framework are acknowledged in section 6. Finally, we summarize our findings in section 7.

2. Model

2.1. Wind velocity profile

Hot stars provide their outer envelopes with plenty of high energy photons able to drive a wind. Most of the predictions from the seminal papers on the theory of radiation-driven winds by Lucy & Solomon (1970) and Castor et al. (1975) have been qualitatively confirmed by observations of isolated hot stars, on the main sequence but also evolved (Puls et al. 2006). In the Sobolev approximation, the radial optical depth can be written as a local quantity modulated by the radial velocity gradient (Sobolev 1960). The wind velocity profile can then be determined analytically and it has been common since then to prescribe, for the dynamics of the wind, a radial velocity profile which obeys the β-law, a generalization of the first analytic formula derived (Puls et al. 2008). Its two parameters are the terminal wind speed v_∞, highly supersonic, and a β exponent which quantifies how quickly the terminal speed is reached :

$$v(r) = v_\infty (1 - R_\star/r)^\beta \qquad (1)$$

where r is the distance to the center of the star and $R_\star$ is the stellar radius. The larger β, the more gradual the acceleration. For the O/B supergiants found in HMXBs, realistic values of the terminal wind speed range from 500 to $2\,000 \mathrm{km \cdot s^{-1}}$.

In Vela X-1, observations of UV spectral lines led Gimenez-Garcia et al. (2016) to propose, for the wind of the donor star HD 77581 of spectral type B0.5Iae (van Kerkwijk et al. 1995), a β-law with $v_\infty \sim 700 \mathrm{km \cdot s^{-1}}$ and $\beta = 1$. Later on, Sander et al. (2017b) computed a hydrodynamic steady-state structure for the wind stratification of the donor star in Vela X-1 based on a non-local thermodynamical equilibrium computation of the population on involved energy levels. Between the photosphere and the compact object and for our current purpose, the velocity profile predicted by Sander et al. (2017b) can be reasonably well fitted by a β-law with $v_\infty \sim 500 \mathrm{km \cdot s^{-1}}$ and $\beta \sim 2.3$. The terminal wind speed in Vela X-1 lies on the lower end of what is usually found in HMXBs, which leads to a wind focused towards the accretor and susceptible to form transient wind-captured disks (El Mellah et al. 2019b), a prediction recently corroborated by observations (Liao et al. 2020). To cite only a few other example HMXBs, in Cygnus X-1, $v_\infty \sim 2\,100 \mathrm{km \cdot s^{-1}}$ (Herrero et al. 1995), in 4U 1700−377, $v_\infty \sim 1\,700 \mathrm{km \cdot s^{-1}}$ (van Loon et al. 2001) and in IGR J00370+6122, $v_\infty \sim 1\,100 \mathrm{km \cdot s^{-1}}$ (Hainich et al. 2020). Given how high the above values for terminal wind speed are compared to the orbital speed in these systems with orbital periods of at least a few days, the wind ballistic streamlines are not significantly curved (El Mellah & Casse 2017). In several HMXBs, the gravitational influence of the compact object has little impact at the orbital scale and the wind should be essentially radial and isotropic around the donor star.

2.2. Clumps

In the two-zones model we work with, all the wind mass is contained in spherical clumps, each being uniformly dense, with an effectively void inter-clump environment. This approximation is justified given the observational findings that most of the mass of the wind material in the two prototypical HMXBs Cyg X-1 and Vela X-1 is concentrated in a small fraction of the volume (Sako et al. 1999; Rahoui et al. 2011). The clumps are carried with the wind, on purely radial orbits. They do not merge with each other, which enables us to use the continuity equation to deduce n, the number of clumps per unit volume at a certain distance r from the stellar center (not to be confused with the particle number density of the smooth wind):

$$n = \frac{\dot{\mathcal{N}}}{4\pi r^2 v} \qquad (2)$$

where $\dot{\mathcal{N}}$ is the rate at which clumps are emitted from the stellar photosphere, given by $\dot{M}/m$. $\dot{M}$ is the stellar mass loss rate and m is the mass of one clump, assumed independent of the distance to the star. All the clumps have the same mass m and the same radius $R_{cl,2}$ at two stellar radii, which are set as input parameters of the model. The evolution of the clump radius with the distance to the star can be set based on observational or physical insights concerning how clumpy the wind is. The latter is quantified through the clumping factor f or the volume filling factor f_{vol}:

$$\begin{cases} f = \langle \rho^2 \rangle / \langle \rho \rangle^2 \\ f_{\mathrm{vol}} = \rho/\rho_{cl} \end{cases} \qquad (3)$$

where ρ is the smooth wind density and ρ_{cl} is the mass density of a clump. When the inter-clump environment is empty, $\langle \rho \rangle = \rho_{\mathrm{cl}} f_{\mathrm{vol}}$ but $\langle \rho^2 \rangle = \rho_{\mathrm{cl}}^2 f_{\mathrm{vol}}$, such that $\langle \rho^2 \rangle / \langle \rho \rangle^2 = 1/f_{\mathrm{vol}} = f$. The radial stratification of the clumping factor around main sequence O stars has been computed by Sundqvist et al. (2018) in 2D radiative hydrodynamics simulations, and around O/B supergiants in 1D setups by Driessen et al. (2019). Observations of isolated O stars yield clumping factors which qualitatively agree with the ones computed from first principles (Puls et al. 2006; Najarro et al. 2011; Sundqvist & Owocki 2013). Representative and numerically-computed profiles of the clumping factor for a set of clump parameters are represented in the bottom panel in Figure 1 (solid lines and shaded regions respectively).

In the case of a uniform clumping factor through the wind, the evolution of the clump radius R_{cl} with the distance r to the stellar center is best represented by:

$$R_{cl} \propto (vr^2)^{1/3} \qquad (4)$$

It is also the profile which ensures that the mass density of constant mass clumps evolves as the density of a smooth wind (Ducci et al. 2010). Alternatively, it has been proposed based on the observed and simulated radial stratification of f in O-stars (Sundqvist & Owocki 2013) that in a simple model such as here the clumps might expand according to (see the Appendix A in Sundqvist et al. 2012):

$$R_{cl} \propto r \qquad (5)$$

Although the exact clump radius expansion law is unknown, radiative hydrodynamics simulations indicate that the radius of the clumps tend to increase as they flow away from the star (Sundqvist et al. 2018). Hereafter, these two expansion laws are referred to as smoothly expanding clumps and as linearly expanding clumps respectively.

The absorption produced by clumps can be quantified through the porosity length, the effective clump column mass divided by the mean density (Owocki & Cohen 2006). The porosity length can be interpreted as the distance in a smooth wind along which the column density is the same as the column density of one clump averaged over all possible impact parameters p:

$$\rho_{cl} \left(\frac{1}{2R_{cl}} \int_{-R_{cl}}^{R_{cl}} 2\sqrt{R_{cl}^2 - p^2} \, dp \right) = \rho_{cl} \frac{\pi}{2} R_{cl} = \langle \rho \rangle h \qquad (6)$$

which means that the porosity length profile can be written as a function of the clumping factor f:

$$h = \frac{\pi}{2} f R_{cl} \tag{7}$$

The profiles for the clump radius, the porosity length, and the clumping factors are shown in Fig. 1 for expansion laws in Eq. (4) and (5) (in blue and red respectively). Linearly expanding clumps lead to a clumping factor peaking at $r = (\beta + 1)R_*$ while in a wind with smoothly expanding clumps, the clumping factor is uniform. Additionally included in the bottom panel in Figure 1 are typical clumping factor profiles obtained from 1D line-driven instability simulations of two O supergiants and two B supergiants (Driessen et al. 2019). We point out that we are not aiming here to obtain absolute clumping factors but rather focus on the comparison with the formalism developed in this paper. Indeed, variations in clumping factor are to be expected between one-dimensional and multi-dimensional line-driven instability simulations (Sundqvist et al. 2018). The latter show that clumping factors are reduced with respect to one-dimensional simulations because the flow is unable to circumvent clumps formed in the simulation (really shells in one dimension). Accelerated interclump matter will flow into dense, clumpy material which artificially increases the clump density ρ_{cl} and, hence, the clumping factor. However, the comparison in Figure 1 indicates that the two expansion laws described above are realistic for the wind of O and B supergiants and that the corresponding clumping factor profiles follow the trends derived by the simulations.

On purpose, we compute the variability of the neutral column density without mentioning the X-ray luminosity itself, the optical depth or the extinction coefficient since the model we develop does not include energy-dependent opacity. In a later paper, we plan to address the question of the ionization structure of the wind, with a proper treatment of the X-ray ionizing feedback from the X-ray source. The present work concerns only the neutral column density, i.e. the amount of material integrated along the LOS, not the absorbing column density deduced from fits of the continuum in X-ray spectra. Changes of the ionization parameter and thus, of the opacity, along the LOS could induce significant variations in the absorbing column density while leaving the neutral column density unchanged (see also discussion in Section 6.2).

2.3. Orbiting X-ray source

In HMXBs, most of the X-rays we observe originate from close to the NS magnetic poles or from close to the innermost regions of the accretion disk surrounding the BH, depending on the nature of the accretor. At the orbital scale, these regions of a few tens to hundreds km are so small that the accretor can be represented as an orbiting X-ray point source in our model.

In classic SgXBs, the eccentricity of the orbit of the compact object is low (Walter et al. 2015). The present model could be extended to include any type of pre-defined orbit but for the sake of simplicity, we only treat circular orbits (see Sect. 6.3 for a discussion on eccentric orbits). The orbit is entirely determined by two parameters: the orbital separation a and the inclination angle i between the line of sight and the orbital angular momentum axis. In Fig. 2 we show two classic HMXBs, Vela X-1 and Cygnus X-1 as seen from Earth. The NS-hosting Vela X-1 is essentially edge-on as it is an eclipsing HMXB, i.e. has a high inclination angle (Joss & Rappaport 1984). The BH-hosting
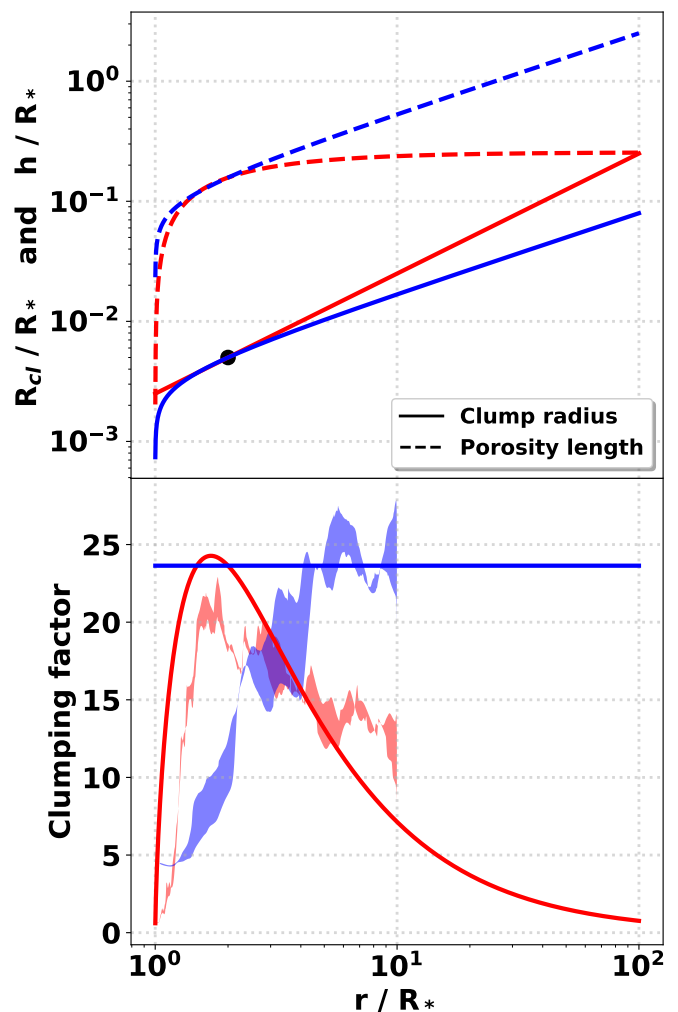
Fig. 1: (top panel) Clump radius (solid lines) and porosity length (dashed lines) in units of R_* as a function of the distance to the stellar center. In blue (resp. in red) are represented the profiles for the clump radius expansion law (4) (resp. (5)). The dimensionless clump radius at $r = 2$, indicated with a black dot, was set to 0.005, and the dimensionless clump mass to $4 \cdot 10^{-7}$ (see section 2.4 for normalization units). (bottom panel) Clumping factor profiles for both expansion laws. The red (resp. blue) shaded region represents the shape of the clumping factor profile obtained for O (resp. B) supergiants by Driessen et al. (2019). Spectroscopically, these OB supergiants can be considered representing typical early- and middle-type stars.

Cygnus X-1 is much more face-on, with a low inclination angle of ~27° (Orosz et al. 2011).

2.4. Physical parameters of the model

Our model includes a very limited number of six degrees of freedom to evaluate the impact of the wind micro-structure on the time variability of the column density. The orbit is determined by the orbital separation a, the orbital inclination i and the orbital period P. The clump properties are the mass and the radius at $2R_*$. The dynamics of the wind is set by the β-exponent. The terminal wind speed v_∞ is used as the normalization quantity for speeds and thus, does not affect the shape of the numerical solutions. The stellar radius R_* is the normalization of the lengths and
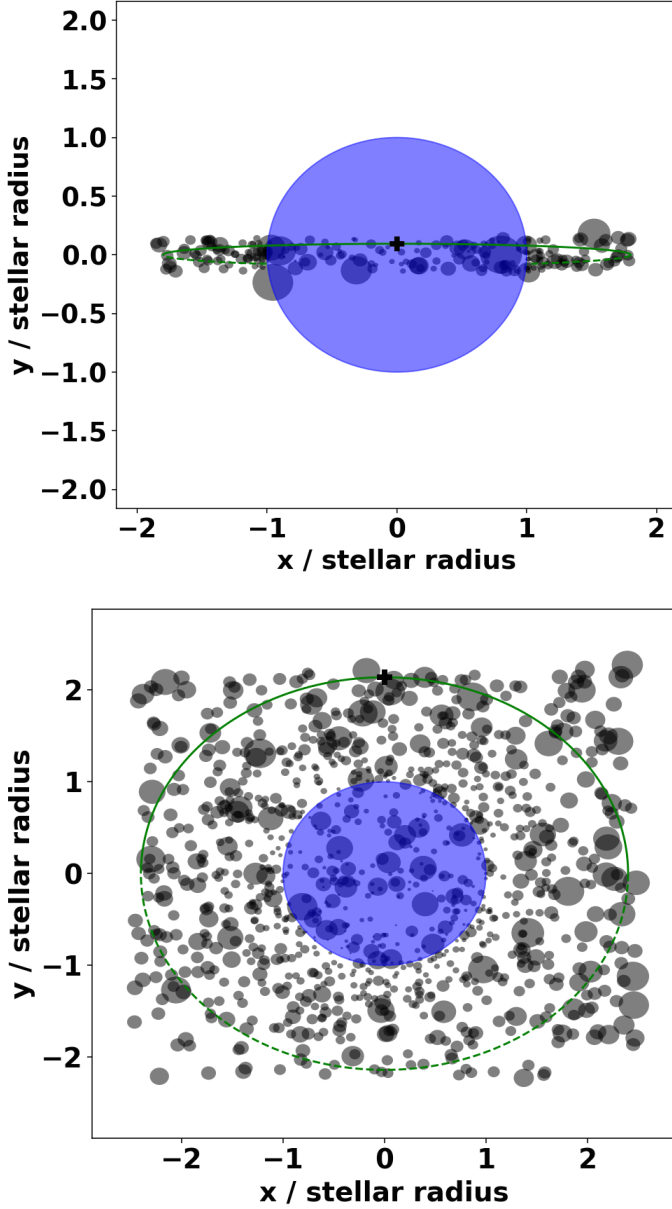
Fig. 2: Representation of the orbit (in green) of the compact object around its stellar companion (in blue) for Vela X-1 (top panel) and Cygnus X-1 (bottom panel) as seen from Earth, where the eccentricity of the orbit has been neglected. Only a fraction of the clumps susceptible to contribute to the column density along the orbit have been represented (in semi-opaque grey). The black cross indicates the point of inferior conjunction on the orbit.

with the stellar mass loss rate $\dot{M}$ as an additional normalization unit, all our results can be scaled to physical units. The scales and their values for two classic HMXBs, Vela X-1 and Cygnus X-1, can be found in Table 1. The values for the six shape parameters we explore are given in Table 2 and correspond to 600 different configurations. From now on, unless specified otherwise, the equations are given in their dimensionless form.

Table 1: Scaling of the model and typical values. In the upper part, the three fundamental normalization units are given for Vela X-1 (from El Mellah et al. 2019b) and Cygnus X-1 (Herrero et al. 1995; Orosz et al. 2011). In the lower part, time, mass and column density normalization units are provided for the two same systems (we assume a mean molecular weight of one proton mass m_p).

HMXBs	Vela X-1	Cygnus X-1
R_*	$28\,R_\odot$	$17\,R_\odot$
v_∞	600 km·s^{-1}	$2\,100$ km·s^{-1}
$\dot{M}$	$6.3{\cdot}10^{-7}\,M_\odot\,$·yr^{-1}	$3.0{\cdot}10^{-6}\,M_\odot\,$·yr^{-1}
$t_0 = R_*/v_\infty$	33 ks	5.7 ks
$m_0 = \dot{M}t_0$	$1.3 \cdot 10^{24}$g	$1.1 \cdot 10^{24}$g
$N_{H,0} = m_0/(m_p R_*^2)$	$2.0 \cdot 10^{23}$cm^{-2}	$4.6 \cdot 10^{23}$cm^{-2}

Table 2: Dimensionless parameters of the model and the values we explore. Normalization units can be found in Table 1.

m_{cl}/m_0	$1{\cdot}10^{-5}, 4{\cdot}10^{-7}$
$R_{cl,2}/R_*$	$0.005, 0.01, 0.02, 0.04, 0.08$
β	$0.5, 2.0$
a/R_*	$1.6, 2, 3$
i	$0°, 25°, 45°, 65°, 90°$
P/t_0	$85, 24$

2.5. Numerics

2.5.1. Clumps

We work in the observer frame centered on the donor star and neglect stellar rotation and wobbling around the center of mass. The latter assumptions are expected to have little impact on the column density variability since the wind essentially flows away from the star, with terminal wind speeds typically larger than the orbital speed by a factor of a few. The position of the clumps is advanced from a lower spherical boundary of radius $r_m = 1.2$ to an upper spherical boundary of radius r_M. Between $r = 1$ and $r = r_m$, the wind is assumed to be smooth, to represent the finite distance from the photosphere beyond which significant clumping is expected (see Fig. 1 for theoretical estimates, and for example Puls et al. 2006, for observational constraints). Clump emission is isotropic in the sense that clumps are injected at the inner boundary $r = r_m$ with an equal probability per solid angle. At each time step, clumps beyond $r = r_M$ are deleted while clumps are created at the basis at a rate $\dot{N} = 1/m_{cl}$. We can estimate a priori the number N of clumps in simulation space by writing:

$$N = \int_{r_m}^{r_M} n4\pi r^2 dr = \frac{1}{m_{cl}} \int_{r_m}^{r_M} \frac{dr}{v} \tag{8}$$

A preliminary integration phase of duration Nm_{cl} guarantees that when we start computing column densities, the whole simulation space is populated with clumps, from the lower to the upper radial boundaries. The position of each clump is advanced using a 4th order Runge-Kutta integration method, with a time step Δt equal to $P/3 \cdot 10^4$. This time step can be compared to the minimum of the duration for a clump to pass in front of a static point source:

$$\Delta t = \min\left[2R_{cl}(r)/v(r)\right] \tag{9}$$

which is found, for both expansion laws, at $r = \beta + 1$. Even in the least favorable configuration, this characteristic time scale
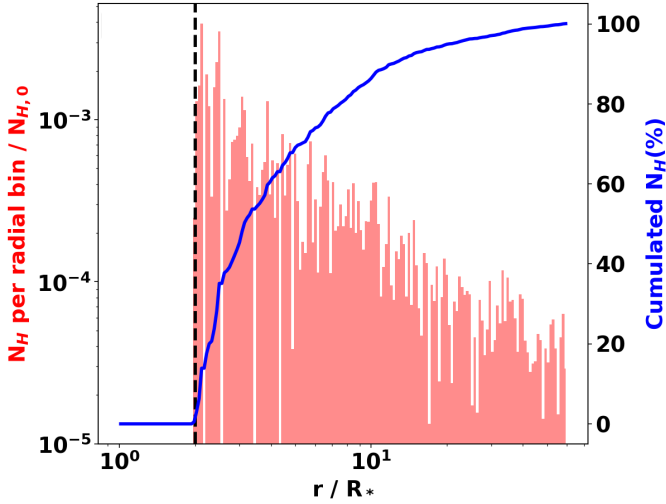
Fig. 3: Column density, per logarithmic radial bin (red, logarithmic axis on the left) and cumulative (blue, linear axis on the right), as a function of the distance to the stellar center. The position of the compact object is indicated with a dashed black line. The total column density up to 30 orbital separations is ∼97% of the column density computed for a smooth wind integrated up to thousands of stellar radii. The dimensionless parameters are $m_{cl} = 10^{-5}$, $R_{cl} = 0.08$, $a = 2$, $P = 80$ and $i = 45°$.

is still hundreds of times larger than Δt, which ensures that we resolve the impact of all clumps on the column density, even the smallest ones with grazing impact parameters with respect to the LOS. For realistic parameters, the total number of clumps can reach up to 10^9 which need to be integrated over $3 \cdot 10^5$ of time steps in order to get the evolution of the column density over 10 orbital periods, our full integration time. In order to reduce the number of clumps and speed up the computation, we retain only the clumps susceptible to intercept the LOS and discard the others. As visible in Figure 2, it means that the number of clumps to consider is much smaller, in particular when the orbit is close to edge-on.

2.5.2. Maximum distance of integration

Every time step, we cast a ray from the X-ray point source to the observer and sum up the contribution of each segment which intercepts a clump to obtain the total column density at this time step. To determine at which distance r_M we should stop the integration of the column density along the LOS, we quantified the contribution of each logarithmic radial bin between the compact object and large distances. We worked at inferior conjunction ($\phi = 0.5$) such as these results are a fortiori valid when the X-ray source is buried deeper into the wind. In Figure 3 is represented the cumulated column density in blue, and the contribution of each bin in red. As we move away from the accretor (located at $r = 2$ in this example), the column density per logarithmic radial bin decreases quickly: 10 orbital separations away from the stellar center, the column density integrated over a certain interval is ∼50 times lower than the one integrated over a range 10 times shorter but around $r = a$. This common trend for all the sets of parameters we considered drove us into setting the outer edge of the simulation domain at $r_M = 30a$, a distance at which the column density has essentially converged.

3. Analytical predictions

3.1. Smooth wind scenario

In the case of a smooth (i.e. homogeneous, without clumps) and isotropic wind with a radial velocity profile which follows a β-law, the normalized column density profile along the orbit of the accretor can be written as:

$$N_H(\phi) = \frac{1}{4\pi} \int_{z(\phi)}^{\infty} \frac{dz}{r^2 (1 - 1/r)^\beta} \tag{10}$$

where r (function of z and of the orbital elements) and z are respectively the distance to the stellar center and the coordinate along the LOS joining the X-ray point source to the observer, both normalized with the stellar radius R_*, and ϕ is the orbital phase (from 0 to 1). This profile depends on three shape parameters and one scale. The three shape parameters are the exponent β of the velocity profile and the orbital elements. For a circular orbit, the latter are the inclination angle i of the orbital angular momentum with respect to the LOS and a, the orbital separation divided by the stellar radius. They both play a role to determine the inferior bound of the integral, $z(\phi)$, which locates the compact object along the LOS, and to convert r into z. The integral can then be performed numerically to compute any column density profile in a smooth and isotropic wind.

Such a fitting procedure grants access to the mass loss rate via the column density scale $N_{H,0}$, provided we can estimate the terminal wind speed and the stellar radius. Due to the conservation of mass, the averaged column density should remain the same whether the mass is gathered in clumps or spread in a smooth wind: the properties of a smooth wind are expected to match the time-averaged properties of a clumpy wind where clumps are realistically small and numerous, a conjecture which will be validated in Section 4.2. The micro-structure of the wind will only manifest through the time variability of the column density.

3.2. Standard deviation

Following the arguments by Owocki & Sundqvist (2018), we may write the variance of the column density between a source located at z_0 along a LOS and an observer at $z = \infty$ as, in physical units and for a mean molecular weight of one proton mass m_p:

$$\delta N_H^2 = \int_{z(\phi)}^{\infty} \left(\frac{\rho}{m_p}\right)^2 h \, dz \tag{11}$$

where h is the porosity length and $\rho = \langle \rho \rangle$ is the mean mass density of the isotropic wind. Using the continuity equation in combination with equation (6), we obtain the dimensionless standard deviation δN_H in column density around the value set by the smooth and isotropic wind as a function of the orbital phase:

$$\delta N_H = \frac{3}{32\pi} \left(m_{cl} \int_{z(\phi)}^{\infty} \frac{dz}{R_{cl}^2 r^2 v}\right)^{1/2} \tag{12}$$

The expansion law for the clumps can then be reinjected in the formula above. For example, for linearly expanding clumps, we then have, if the velocity profile is given by the β-law (1):

$$\delta N_H = \frac{3}{8\pi} \left(\frac{m_{cl}}{R_{cl,2}^2} \int_{z(\phi)}^{\infty} \frac{dz}{r^4 v}\right)^{1/2} \tag{13}$$

This shows explicitly how, for a given orbit and wind acceleration, the standard deviation of the column density depends on the ratio $\sqrt{m_{cl}}/R_{cl,2}$ for any power-law clump radius expansion.

We performed simulations with both clump radius expansion laws for the 300 simulations with high-mass clumps ($m_0 = 10^{-5}$), less computationally-demanding due to the lower total number of clumps in the simulation space. The results were similar enough that all the conclusions we draw in the next sections are equally valid for both laws. It was to be expected because in addition to the expression (12) above, Figure 1 indicates that clump radii and porosity lengths within $3R_*$, in the region where the clumps contribute the most to the final column density, are alike. Hereafter, results are presented for the smoothly expanding law (4).

4. Results

4.1. Time evolution of the column density

The main output of each simulation is a time series of the column density. This data is represented for three simulations in Figure 4 over a few orbital periods. As the compact object orbits the donor star, the amount of material integrated along the LOS changes because of two effects: the motion of the X-ray point source around the star and the clumps crossing the LOS. The latter induces a variability on short time scales whose statistical properties relate to the micro-structure of the wind and are discussed in more detail in Sections 4.2 and 4.3. The orbital motion, on the other hand, provokes a smooth periodic modulation of the column density, more contrasted for higher inclination and orbital separation, and which vanishes for face-on configurations where the distance between the accretor and the observer remains constant (see bottom panel in Figure 4). At high inclination, eclipses can occur during which the column density can not be measured (see gaps in the top panel in Figure 4, for a 90° inclination). The duration d of an eclipse with respect to the orbital period P relates to the ratio a/R_* via:

$$\frac{d}{P} = \frac{1}{\pi} \arcsin\left(\frac{R_* \sin i}{a}\right) \sim \frac{1}{\pi}\frac{R_* \sin i}{a} \tag{14}$$

where the approximation is valid within 10% percent for any inclination provided $a > 1.6R_*$, a condition usually met in HMXBs (e.g., Falanga et al. 2015). In Figure 4, we represented the smooth wind solution obtained with equation (10) with a dashed green line. The measured column densities oscillate around this profile. Because we only cover the case of circular orbits in this paper, the smooth wind as a function of the orbital phase ϕ is symmetric with respect to the axis $\phi = 0$ and $\phi = 0.5$ (superior and inferior conjunction respectively). We highlighted the short term variability of the column density with inserts showing zoomed-in versions of the time series. Each insert contains approximately 200 data points which are visible and indicate that the impact of the clumps is resolved up to very short time scales. The total column density consists of cumulative contribution of many clumps with different radii and densities, which indicates that accurate knowledge on the clumpiness of the stellar wind can be gained from the time variability of the column density.

4.2. Column density peak-to-peak variability

4.2.1. Variability amplitude as a function of the orbital phase

In Figure 4, the spread of the column density around its smooth wind value changes from a simulation to another. In this section,

we determine the main parameters which set the measured standard deviation but beforehand, we represent the column density as a function of the orbital phase in Figure 5. We computed the column density during each simulation at 50 locations equally spaced on the orbit simultaneously every 100 time steps such as each orbital phase bin in Figure 5 contains 6 000 values of N_H (after folding the orbit from $\phi = 0$ to $\phi = 0.5$). For each bin, we compute the median (black steps) and the standard deviation. The black shaded region around the median shows the values between the 20th and the 80th percentiles while the grey shaded region is delimited by the 5th and the 95th percentiles. Simultaneous computation of N_H along the orbit enables us to get a much better statistics to compute the standard deviation at each orbital phase than using the time series presented in Section 4.1. It does not introduce biases due to time coherence of the signal associated to clumps if the simulation duration (ten orbital periods) is high compared to the coherence time scale, an assumption we validate a posteriori (see Section 4.3). These results indicate that except for very large ($R_{cl} = 0.08$) and sparse clumps ($m_{cl} = 10^{-5}$), the median N_H profile is representative of the smooth wind profile with the same parameters but where clumps are replaced with a smooth wind of same mass loss rate.

4.2.2. Comparison to analytical predictions

For each simulation, we compared the profiles of the standard deviation as a function of the orbital phase to the predicted profiles derived in Section 3.2 (see Figure 6). Apart near superior conjunction in a few configurations, they match within a few percent. The discrepancies sometimes observed near superior conjunctions can be fully attributed to two numerical artifacts. First, when the system is eclipsing, the orbital bin which contains ingress or egress underestimates the variability because it averages the standard deviation over a finite orbital phase interval which partly includes the eclipse, during which there is no variability. Second and more importantly, when the LOS intercepts the region $r \in [1; 1.2]$ around the donor star where we assumed that the wind is smooth, the standard deviation is also lowered with respect to the prediction of the analytical model where the wind is assumed to be clumpy all the way down to the stellar photosphere. Observational hints in favor of clumpiness near the star exist (Puls et al. 2006; Cohen et al. 2011; Torrejón et al. 2015) but our model provides a way to quantify this: if the standard deviation at superior conjunction measured in HMXBs where the orbis is grazing is lower than what predicted from fitting the standard deviation profile far from superior conjunction with the formula (11), then it would support the scenario of a smooth wind basis.

4.2.3. Dependence on parameters

Finally, we compare the standard deviation of the column density at inferior and superior conjunctions, $\delta N_{H,inf}$ and $\delta N_{H,sup}$, for different parameters. The dependency of δN_H on $\sqrt{m_{cl}}/R_{cl}$ in equation 11 invited us to represent $\delta N_{H,inf}$ and $\delta N_{H,sup}$ as a function of $\sqrt{m_{cl}}/R_{cl,2}$ in the left column in Figure 7 for an orbital inclination of 65°, 25° and 0° (top, middle and bottom rows). For eclipsing HMXBs, the standard deviation at superior conjunction is not defined and thus not represented. We vary the orbital separation (different markers) and differentiate quickly and slowly accelerating winds (filled and empty markers respectively). In blue (resp. red) are shown the values of $\delta N_{H,sup}$ (resp. $\delta N_{H,inf}$). These results do not depend on the orbital period, which
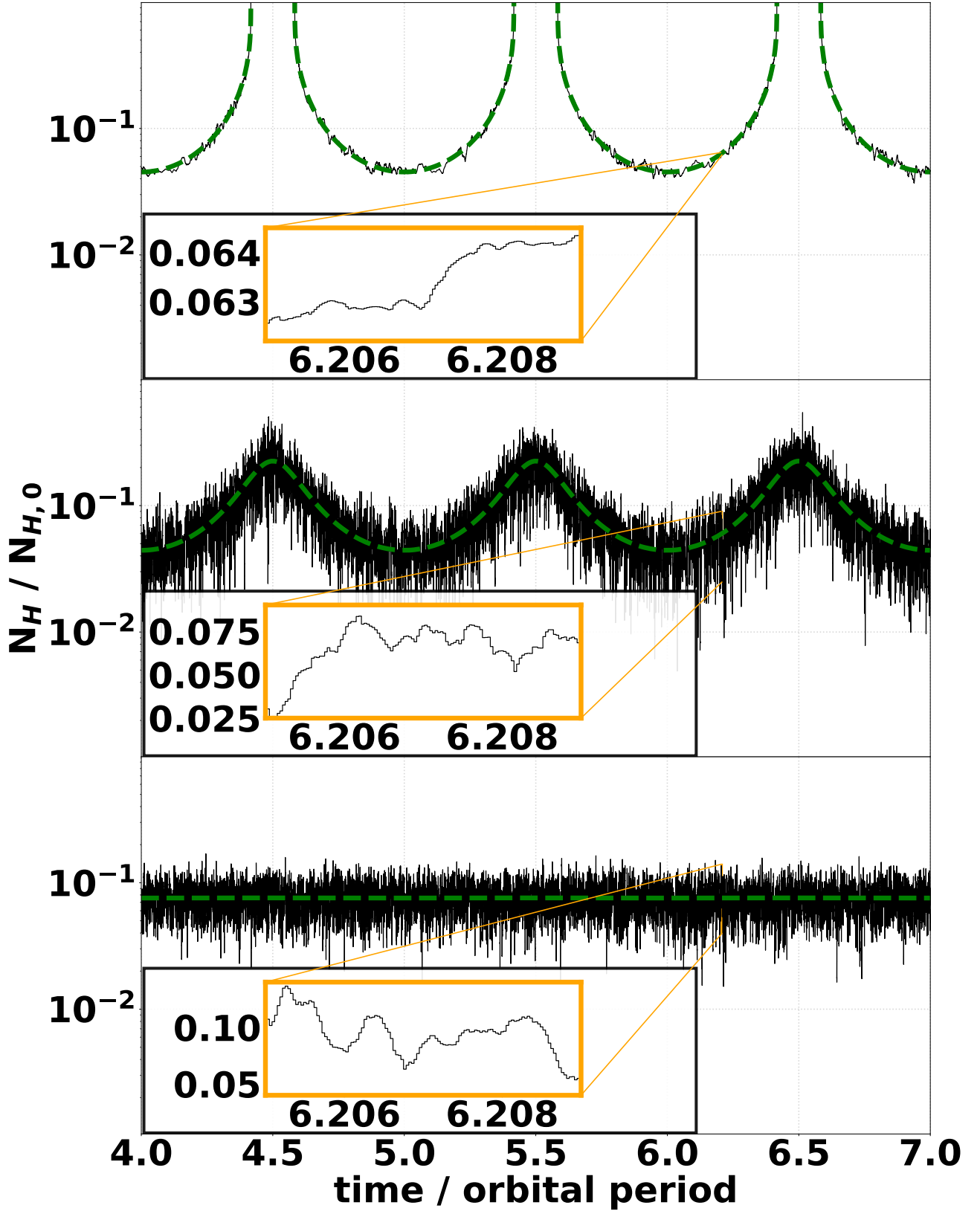
Fig. 4: Three different evolutions of the column density as a function of time over several orbits for $i = 90°$ (top panel), $i = 45°$ (middle panel) and $i = 0°$ (bottom panel) - and different clump radii, masses, orbital separations, periods and β exponent. The dashed green line is the corresponding smooth wind column density profile. The top profile displays eclipses due to the high inclination. The insets show zoomed in portions of the curves and the numerical time sampling of the column density, $3 \cdot 10^4$ times per orbital period, is visible. The origin of time is set at inferior conjunction (i.e. $t = 0$ at $\phi = 0.5$).
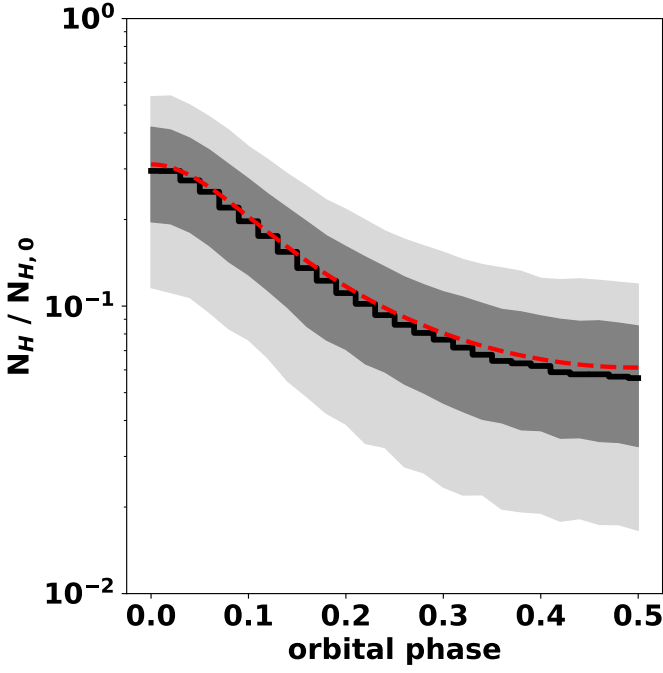
Fig. 5: Column density from superior conjunction ($\phi = 0$) to inferior conjunction ($\phi = 0.5$) for an orbital inclination $i = 45°$. In black is represented the median over 10 orbits and the red dashed line is the smooth wind solution from equation 10. The dark (resp. light) grey shaded region is bounded by the 20th to 80th percentiles (resp. the 5th to 95th percentiles). The parameters are $m_{cl} = 10^{-5}$, $R_{cl} = 0.01$, $\beta = 0.5$ and $a = 2$.
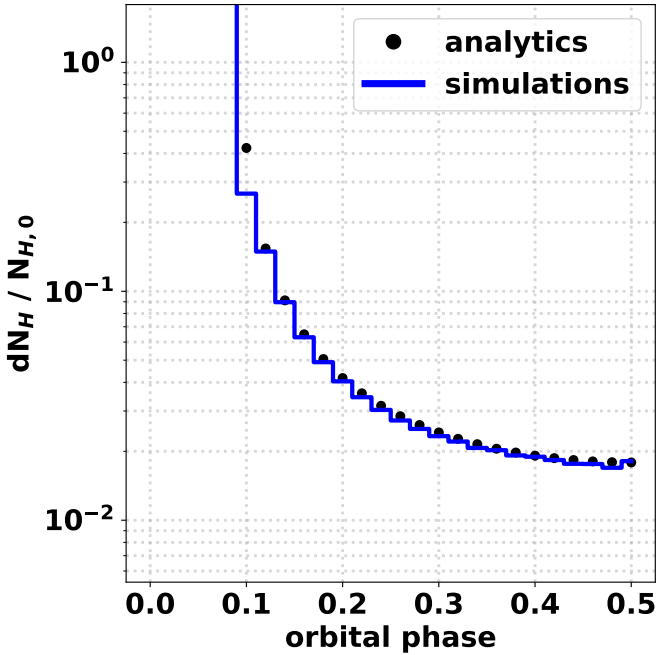

Fig. 6: Standard deviation of the column density as a function of the orbital phase computed numerically (in blue) and analytically (black dots) for a simulation with $m_{cl} = 10^{-5}$, $R_{cl} = 0.02$, $\beta = 2$, $a = 2$ and $i = 90°$. The discrepancy at egress is partly indicative of the region near the stellar photosphere where the wind is not clumpy yet.

was expected since the orbital period is so much longer than the timescale at which N_H varies. All other parameters being fixed, we see that the relation $\delta N_H \propto \sqrt{m_{cl}}/R_{cl,2}$ whose slope is indicated in the first panel with a black dashed line is verified for each set of ten points (five different values of $R_{cl,2}$ and two values of m_{cl}). The ratio between the standard deviation at superior and inferior conjunctions is hardly sensitive to the orbital separation. As the orbital separation increases, the difference between slowly and quickly accelerating winds vanish at inferior conjunction: while the wind speed at $r = 1.6$ is more than four times higher for $\beta = 0.5$ than for $\beta = 2$, this ratio drops to less than 2 at $r = 3$. The difference between $\beta = 0.5$ and $\beta = 2$ remains significant at superior conjunction though, even for $r = 3$, since the LOS probes regions $r < a$ enclosed within the orbit. A higher β leads to a higher standard deviation due to the higher number of clumps per unit volume at a given distance from the star (see equation (2)). The standard deviation at superior conjunction is always higher than at inferior conjunction, except for face-on orbits where they coincide: at superior conjunction, the LOS intercepts a region closer from the star than at inferior conjunction, where the clumps are small and packed, which increases the standard deviation.

Given the dominating contribution of the densest clumps pinpointed in Figure 3, we changed the clump radius used in the x-axis of the plots in Figure 7 so as it corresponds to the smallest clump radius encountered along the LOS, $R_{cl,min}$, i.e. the clump radius at the point along the LOS the closest from the donor star (right column in Figure 7). At inferior conjunction, this point is simply the position of the compact object but at superior conjunction, it is a point located deep in the wind if the inclination is significantly high. This correction enables us to get a much lower dispersion of the points along the $\delta N_H \propto \sqrt{m_{cl}}/R_{cl,min}$ axis and proves that the standard deviation is an excellent tracer of the ratio $\sqrt{m_{cl}}/R_{cl,min}$. Once the parameters a, i, β and $N_{H,0}$ have been constrained thanks to the median column density profile as a function of the orbital phase, a precise measure of the standard deviation grants us access to the ratio $\sqrt{m_{cl}}/R_{cl,min}$. The accuracy of this obtained ratio is maximal if δN_H is measured at inferior conjunction, where the dispersion is the lowest. The latter effect can be explained by the fact that at inferior conjunction, the LOS is best aligned with the radial direction from the donor star (with exact alignment for an edge-on system) so the column density is mostly localized near the accretor and the contributions quickly drop as we go towards the observer. Another advantage of working at inferior conjunction is to obtain an accurate median profile $N_H(\phi)$ with fewer observations. The spread which subsists in the right column in Figure 7 is due to the minor but non negligible contribution of clumps with radii $R_{cl} > R_{cl,min}$ on the standard deviation of the column density.

These results illustrate how the standard deviation on column density can be exploited to constrain the ratio $\sqrt{m_{cl}}/R_{cl,min}$, or alternatively the porosity length since $\sqrt{m_{cl}}/R_{cl} \propto \sqrt{h}$. In order to disentangle the clump mass and radius, it is necessary to analyze another output of our simulations, the coherence time scale.

4.3. Coherence time scale

4.3.1. Autocorrelation function

In the previous section, we extracted the information on the characteristic standard deviation of the column density at each orbital phase for each set of parameter, but we did not exploit the information on the time evolution of the column density. Obervations of HMXBs with X-ray satellites are often carried out over inter-
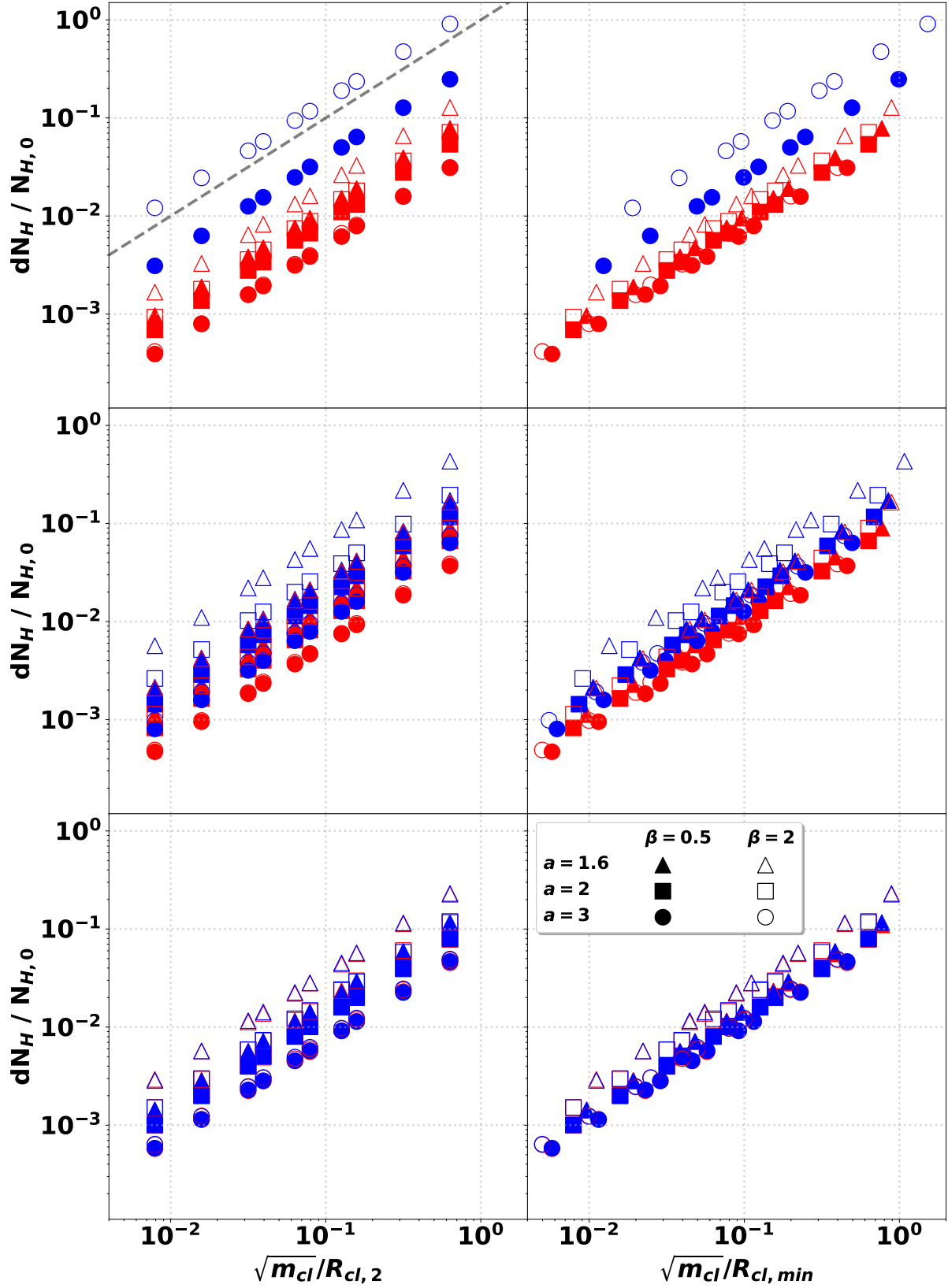
Fig. 7: From top to bottom row, the orbital inclination is 65°, 25° and 0°. (left column) Standard deviation of the column density at inferior (resp. superior) conjunction in red (resp.blue) as a function of the ratio $\sqrt{m_{cl}}/R_{cl,2}$. Each couple (a, β) leads to a different proportionality constant between δN_H and $\sqrt{m_{cl}}/R_{cl,2}$, hence the large dispersion. The dashed line in the top left panel indicates the $y = x$ line. (right column). Same as before but $R_{cl,2}$ has been replaced by the clump radius at the point along the LOS between the X-ray source and the observer the closest from the donor star. The dispersion is reduced, especially at inferior conjunction.
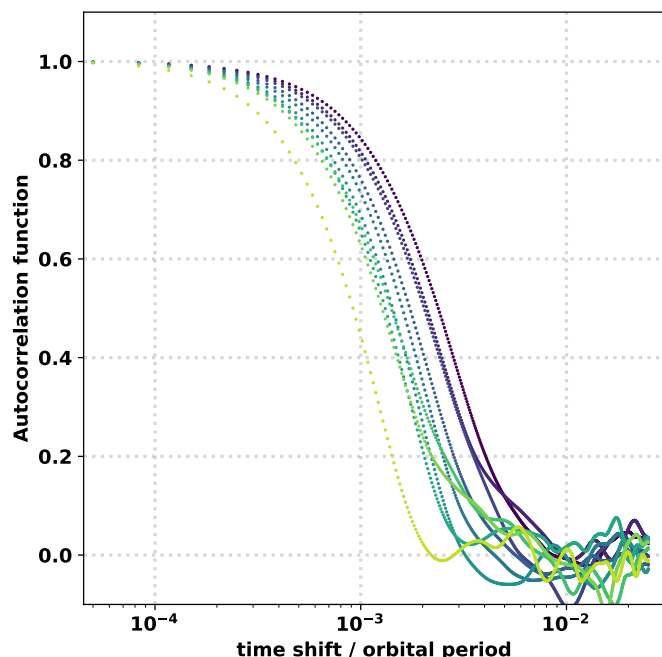
Fig. 8: Autocorrelation function of the column density as a function of the time shift. From purple to green and yellow, we represent the autocorrelation functions of the data at different orbital phases, from inferior conjunction (dark purple) to superior conjunction (yellow). Simulation with $m_{cl} = 4 \cdot 10^{-7}$, $R_{cl} = 0.04$, $\beta = 2$, $a = 3$, $i = 65°$ and $P = 85$.
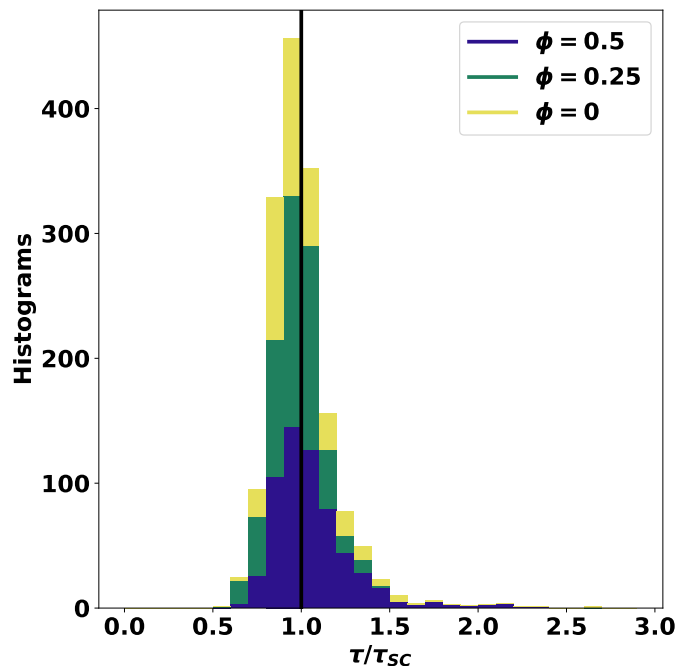

Fig. 9: Stacked histograms of the ratios of the measured coherence time scale τ compared to the clump self-crossing time τ_{SC} for all 600 simulations at inferior conjunction ($\phi = 0.5$, purple), $\phi = 0.25$ (green) and superior conjunction ($\phi = 0$, yellow).

vals of time lasting for a significant fraction of the orbital period (e.g., Haberl et al. 1989; Odaka et al. 2013; Miškovičová et al. 2016; Grinberg et al. 2017). From such a continuous X-ray observation of a HMXB, the column density as a function of time can, in theory, be extracted on sufficiently short timescales. The time series contain an additional information which is the coherence time scale, the characteristic duration over which the changes in column density are smooth and, on average, predictable[1].

In order to determine the coherence time scales in each simulation, we first compute the relative difference between the time series presented in Section 4.1 and the smooth wind solution (10), and subtract the median of the obtained signal afterwards. Since we expect the coherence time scale to vary with the orbital phase, we must treat separately the different orbital phases to avoid smearing out the coherence time scale. We cut the time series in twenty equal orbital phase intervals. In spite of the motion of the X-ray source along its orbit, we can still use the symmetry with respect to $\phi = 0.5$ and gather the data at $\phi = 0.25$ and $\phi = 0.75$ for instance, since both are expected to have the same coherence time scale. For each simulation, we are left with ten orbital phase intervals of width 0.05, between $\phi = 0$ and $\phi = 0.5$, each containing twenty time series of the column density of duration $P/20$. The autocorrelation function of each of this individual time series is then computed and the twenty autocorrelation functions of each orbital phase bin are averaged to obtain a representative autocorrelation function for each of the ten intervals. With this method, we can capture coherence time

scales ranging from $P/(3 \cdot 10^4)$ (the time resolution) up to $P/40$. As an illustration, the ten autocorrelation functions of a fiducial simulation are represented in Figure 8, from inferior conjunction (dark purple) to superior conjunction (yellow).

The autocorrelation function is maximal in zero since the time series is fully correlated to its zero time shifted counterpart. As the shift increases, the correlation decreases until the time shift is so large that the two functions are no longer correlated at all. The coherence time scale corresponds to the time beyond which the signal changed enough to consider that it lost the memory of its previous values. We measure it by taking the time shift when the autocorrelation has been halved, τ. We evaluate the uncertainty on the obtained value of τ by looking at the face-on configurations, where τ should not depend on the orbital phase: it remains indeed constant, and varies by at much 5%.

The coherence time scale measured at inferior conjunction is typically higher than the one at superior conjunction. The LOS probes deeper wind layers at superior conjunction where clumps are smaller but also slower, such that a shorter coherence time scale is not obvious without accounting for the orbital speed, which turns out to be larger than the speed of the clumps near the stellar photosphere.

4.3.2. Dependence on parameters

In this section, we focus on the coherence time scales computed in bins centered on phases $\phi = 0$, $\phi = 0.25$ and $\phi = 0.5$ and of width 0.1 each. To study the evolution of the coherence time scale with the parameters, we want to compare the coherence time scale τ to the amount of time a single clump intercepts the LOS to the accreting compact object i.e. the duration for the X-ray source to cross a clump projected along the LOS. We call it the self-crossing time and write it τ_{SC}. Due to the short orbital periods and the high total masses in HMXBs, the orbital speed

---

[1] We note that while we employ the autocorrelation function here, an alternative but mathematically equivalent approach using power density spectra to assess the characteristic timescales of variability can be applied.

can be as high as a few hundreds of kilometers per second. This speed is not negligible compared to the speed of the wind, especially if the acceleration is very gradual (i.e. high β). We compute the local relative speed Δv between the orbiting X-ray point source and the densest clumps along the LOS:

$$\Delta v = [v_{orb}^2 \left(1 - \sin^2 \Phi \sin^2 i\right) + v_{cl}^2 \left(1 - \cos^2 \Phi \sin^2 i\right) ...$$
$$... - 2v_{orb}v_{cl} \cos \Phi \sin \Phi \sin^2 i]^{1/2} \quad (15)$$

where $\Phi = 2\pi\phi$, $v_{orb} = 2\pi a/P$ and $v_{cl} = v(r = a)$. From this, we deduce the self-crossing time:

$$\tau_{SC} = 2R_{cl}/\Delta v \quad (16)$$

To compute the clump radius R_{cl} which enters this equation, we focus on the clumps which contribute the most to N_H, like we did in section 4.2.3: at inferior conjunction and $\phi = 0.25$, we compute the clump radius at $r = a$ while at superior conjunction, we compute the clump radius at the point along the LOS which is the closest from the donor star.

Figrue 9 provides an overview of the ratios τ/τ_{SC} for all simulations. Except for a handful of simulations where clumps are the largest and the scarcest, the coherence time scale matches the self-crossing time within 50%. This result means that a fairly accurate estimate of the clump self-crossing time and, by then, of the characteristic dimension of the clumps, can be obtained by measuring the full width at half maximum of the autocorrelation function of a column density time serie. Within the ranges of parameters we explored, τ_{SC} depends on all the 6 dimensionless parameters summarized in Table 2 except on the clump mass. It provides a convenient way to distinguish the size and the mass of the clumps, which were intertwined when we analyzed the standard deviation on column density in Section 4.2. The mean N_H profile serves first to constrain the 4 other parameters (a, i, P and β). Then, the coherence time scale, via τ_{SC}, tells us about the dimension of the smallest clumps along the LOS, $R_{cl,min}$, and the standard deviation provides insights on the ratio $\sqrt{m_{cl}}/R_{cl,min}$. The mass of the clumps can then be estimated using purely the time variability of the column density and independently from any accretion diagnostics.

5. Observational diagnostics

5.1. Procedure

5.1.1. Time-averaged wind

The procedure we propose to determine the clump properties from the variability of the column density requires first to have constrained values for the orbital inclination i and separation a, the shape of the velocity profile (i.e. the β-exponent) and the column density scale N_{H_0}. This preliminary step makes use of the good match between the smooth wind profile and the time-averaged profile of the column density (see Section 4.2).

To illustrate how these first parameters could be obtained, we focus on an actual HMXB. The classic SgXB 2S0114+650 (also known as LSI+65 010) is an excellent candidate to apply the model presented in this paper, thanks to its intermediate orbital inclination. Sanjurjo-Ferrrín et al. (2017) provide a ratio a/R_* of 1.34-1.65. Given the high mass ratio (Reig et al. 1996), the absence of accretion disk (Koenigsberger et al. 2003) and the moderate X-ray luminosity ($1.4 \cdot 10^{36}$erg $\cdot$ s^{-1}, Sanjurjo-Ferrrín et al. 2017), we can safely assume that the star does not fill its Roche lobe. It brings us to the conclusion that the upper limit of this range is to be preferred for the ratio a/R_*. Pradhan et al. (2015)

showed that it was not eclipsing by measuring a finite column density at superior conjunction. However, the sharp decrease of the column density following superior conjunction indicates that the LOS probes deep layers of the wind, near the photosphere. Consequently, the orbital inclination has to be between 40° and 50° approximately, which is also consistent with results obtained from radial velocity measures of the donor star (Crampton et al. 1985; Farrell et al. 2008; Koenigsberger et al. 2006). We fitted the N_H data between orbital phases 0 and 0.1 reported in Pradhan et al. (2015) with the smooth wind profile given by equation (10). We could find a reasonable match for the following parameters: $a = 1.6$, $i = 50°$, $\beta = 1$ and $N_{H,0} = 1.2 \cdot 10^{23}$cm^{-2}. Reig et al. (1996) estimated the terminal wind speed to be $1\,200$km$\cdot$s^{-1}, such that if the stellar radius is $R_* = 25$R$_\odot$, we deduce from $N_{H,0}$ a stellar mass loss rate $\dot{M} \sim 7 \cdot 10^{-7} M_\odot$ yr^{-1}, very similar to the mass loss rate of the donor star in Vela X-1 (Giménez-García et al. 2016).

Investigations of the stochastic properties of the column density along the orbit would be a precious element to gain knowledge on the size and mass of the clumps in the wind of the B1 supergiant donor star in 2S0114+650. The moderate X-ray luminosity of the accretor ensures that an accurate value of the neutral column density can be derived from the X-ray absorption (see discussion on the X-ray ionizing feedback in Section 6). This example shows how the average N_H profile as a function of the orbital phase can be helpful in order to constrain the β-exponent of the wind velocity profile, the scale $N_{H,0}$ and the orbital parameters. Spectral characterization in the optical and UV waveranges of the stellar atmosphere with non local thermodynamical equilibrium analysis can bring additional constrains to break the degeneracy and disentangle between the different parameters (Hainich et al. 2020). In eclipsing HMXBs, the median N_H profile at egress is the most constraining while an accurate ratio $(R_*/a) \sin i$ can be determined from the eclipse duration from Equation 14.

5.1.2. Clump masses and radii

Once the fundamental parameters of the problem have been constrained thanks to the median column density profile and possibly additional insights (e.g. radial velocity profiles or the extent of the stellar Roche lobe), the N_H time series provided by time-resolved X-ray spectroscopy can be used to determine the mass and the spatial extent of the clumps. The latter manifests as a coherence time scale imprinted in the signal which can be extracted using the autocorrelation function. It typically ranges from a few 10^{-4} to a few 10^{-2} times the orbital periods, which means that a time resolution of ~ 100 seconds is enough to determine the clump radius if a coherence time scale is detected, and to provide constraining upper limits on the size of the clumps otherwise. The relative speed projected on the plane of the sky of the clumps with respect to the X-ray point source is lower near inferior conjunction. For systems where the inclination is low enough that we can afford it ($i < 65°$), measures at inferior conjunction should be privileged since they yield longer coherence time scales. Otherwise, measures at $\phi \sim 0.2 - 0.3$ are to be preferred.

While a corresponding observational analysis is out of scope of this paper, we point towards several observational X-ray studies of HMXBs achieving measurements of variable absorption on required or slightly larger timescales. In the eclipsing HMXB Vela X-1, absorption has been directly modelled at different orbital phases on timescales of ~ 1 ks using *Suzaku* (Odaka et al. 2013) and *XMM-Newton*'s EPIC-pn (Martínez-
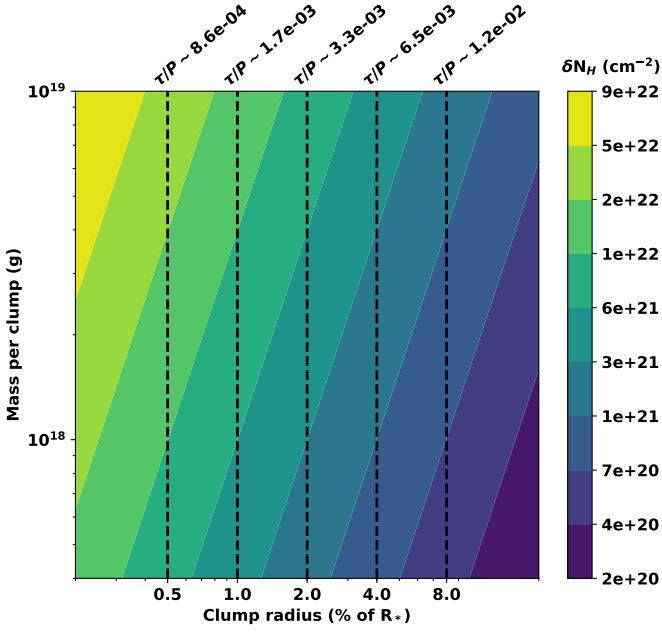
Fig. 10: Synthetic diagram summarizing the dependence of the coherence time scale τ and of the standard deviation on the column density δN_H on the size of the clumps and their mass, for intermediate parameters ($a = 2$, $i = 45°$, $P = 24$ and $\beta = 2$). We used as normalization units $m_0 = 10^{24}$g for masses and $N_{H,0} = 3 \cdot 10^{23}$cm^{-2} for column densities.

Núñez et al. 2014) and on timescales of individual pulsar pulses, i.e. ~ 280 s, using *NuSTAR* (Fürst et al. 2014). The variability in 4U 1700−37 has been studied by Haberl et al. (1989) on timescales of ~ 1 ks. In general, in bright sources, such as Cyg X-1, the variability of absorption may be accessible on even shorter timescales even with current instruments using color-color diagrams (Nowak et al. 2011; Hirsch et al. 2019, Grinberg et al. in prep.), although exact measurements are yet lacking in the literature. High throughput X-ray missions such as *XRISM* (XRISM Science Team 2020), *eXTP* (in't Zand et al. 2019), and *Athena* (Nandra et al. 2013) will enable even better measurements on short timescales and make a high number of fainter sources accessible for short-term absorption variability studies.

The coherence time scale obtained from the width of the autocorrelation function at half its maximum is a reasonably accurate measure of the clump crossing time (Sec. 4.3). To this extent, the β exponent and the orbital parameters grant access to an estimate of the clump radius at a distance from the donor star $r \gtrsim a$ for coherence time scales measured between $\phi = 0.25$ and 0.5, and at a distance $r < a$ for measures at $\phi = 0$ to 0.25.

The coherence time scale is insensitive to the mass of the clumps. At a given stellar mass loss rate, provided most of the mass is contained in the clumps, a higher clump mass means a lower number of clumps per unit volume and, by then, a higher clumping factor. The photon mean-free-path is longer, and so is the porosity length. The latter quantity provides an analytic prediction for the standard deviation of the column density, δN_H, which turns out to be accurate within a few percent (see Section 4.2.2). At inferior conjunction, $\delta N_H/N_{H,0}$ provides a direct measure of the ratio $\sqrt{m_{cl}}/R_{cl}$ whose accuracy is within a factor of 2 in the worst case, when no other parameter (a, i, P and β) is known (see Figure 7). Since the clump radius R_{cl} entering this

ratio is the same as the one deduced from the coherence time scale, the characteristic mass of a single clump can be derived.

The diagram in Figure 10 summarizes the main ideas underlying this procedure for observational diagnostics of the wind micro-structure, showing the relationship between the mass of an individual clump, clump radius and the standard deviation of the column density δN_H, here calculated for a special case. For illustrative purposes and to provide masses in physical units, we considered arbitrary scaling units and a simulation with intermediate parameters. The coherence time scales τ are given in orbital periods and directly map for clump radii. The additional information on δN_H enables to constrain the range of possible clump masses using:

$$
m_{cl} \sim 3 \cdot 10^{22}\text{g} \left(\frac{R_{cl,m}}{R_*}\right)^2 \times ...
$$
$$
\left(\frac{R_*}{20R_\odot}\right)^3 \left(\frac{v_\infty}{1\,000\text{km} \cdot \text{s}^{-1}}\right) \times ...
$$
$$
\left(\frac{\dot{M}}{10^{-6}M_\odot \cdot \text{yr}^{-1}}\right)^{-1} \left(\frac{\delta N_H}{5 \cdot 10^{21}\text{cm}^{-2}}\right)^2 \tag{17}
$$

The corresponding porosity length is, for the parameters and mass unit used in Figure 10:

$$
h \sim 2\%R_* \left(\frac{m_{cl}}{4 \cdot 10^{17}\text{g}}\right) \left(\frac{R_{cl,2}}{0.01R_*}\right)^{-2} \tag{18}
$$

This small value of the porosity length is typical of an environment with many low mass clumps susceptible to intercept the LOS and capture photons.

5.2. Comparison to previous results for clumps in HMXBs

For clump sizes and masses chosen based on radiative hydrodynamics simulations ($R_{cl} \sim 0.01R_*$ and $m_{cl} \sim$ a few 10^{17}g, Sundqvist et al. 2018), the dispersion of the N_H values around the smooth wind profile is limited. The clumps with masses $m_{cl} \sim 10^{22-23}$g and radii $R_{cl} \sim$ a few $R_*/10$ deduced from hard X-ray flares in SFXTs (Walter & Zurita-Heras 2007), which trace the intrinsic emission and thus, the mass accretion rate, are more likely unrelated to the capture of a single clump by the compact object. Instead, they could be due either to large scale structures crossed by the accretor (e.g. co-rotating interaction regions, Bozzo et al. 2017) or either to instabilities and gating mechanisms at the outer rim of the NS magnetosphere such as the propeller effect (Bozzo et al. 2008; Parfrey & Tchekhovskoy 2017), or within the accretion disk surrounding the black hole. For the edge-on HMXB Vela X-1, Grinberg et al. (2017) carried out a time-resolved analysis of the X-ray spectra and identified two coherent episodes of enhanced absorption of approximately an hour each, which would correspond to clumps of size $R_{cl} \sim 5\%R_*$. However, the amplitude of the N_H increase, of several 10^{22}cm^{-2}, is too high to be explained by clump-induced stochastic variations. In edge-on systems, these observations could be due to variability in the accretion wake or, when observations are performed at $\phi \sim 0.25$ like in Grinberg et al. (2017), to the formation of transient high density structures around the NS magnetosphere such as an accretion disk (El Mellah et al. 2019a; Liao et al. 2020) or a quasi-spherical shell (Shakura et al. 2013).

6. Limitations of the model

6.1. Caveats for edge-on systems

Since the first simulations of wind accretion by Blondin et al. (1990), the flow in HMXBs is believed to form, in the orbital plane, a hydrodynamics bow shock which trails the accreting compact object due to the orbital motion. Manousakis & Walter (2015) showed that this dense structure was highly variable due to the X-ray ionizing feedback from the accretor onto the feeding material upstream, which alters the line acceleration as first described by Hatchett & McCray (1977) (see Section 6.2). We intentionally left large scale density modulations out of the model introduced in the paper so as to isolate the effect of the clumps themselves on the variability of the column density. In order to apply the present model in HMXBs with high orbital inclination (eclipsing and/or $i > 65°$), observations from superior conjunction ($\phi = 0$), or egress if eclipsing, up to $\phi \sim 0.2 - 0.3$ are relevant to determine the wind micro-structure. In this interval, the accretion wake points away from the observer and does not intercept the LOS. Elsewhere, the column density is significantly impacted by the contribution of structures not associated to the clumps. Instead, for intermediate inclinations ($25° < i < 65°$), data up to inferior conjunction can safely be used, especially if the wind speed is large compared to the orbital speed, leading to a low opening angle of the bow shock around the accretor. If the inclination is low ($i < 25°$), X-ray data at any orbital phase can be used but the weak modulation of photometric and spectroscopic signals with the orbital motion makes quantities such as the orbital period difficult to narrow down. Notice that a low inclination is much less likely than an edge-on configuration since the probability to observe a system with orbital inclination i goes as $\sin i$.

6.2. X-ray photoionization

Wind accretion being less efficient at transferring stellar material to the compact object than Roche lobe overflow, the mass accretion rate in wind-fed HMXBs is generally moderate, leading to typical X-ray luminosities of the order of $10^{36} \mathrm{erg \cdot s^{-1}}$. Nevertheless, the influence of the X-rays emitted from the immediate vicinity of the compact object on the ionization state of the upstream wind can often not be neglected (see e.g., Boroson et al. 2003; Miškovičová et al. 2016, for observational results). In addition of altering the wind dynamics (e.g., Čechura et al. 2015; Sander et al. 2017b), the X-rays ionize the material surrounding the compact object and significantly decreases its opacity (Hatchett & McCray 1977; Ho & Arons 1987). In particular in the soft X-ray range used for absorption measurements in HMXBs, the effects of changing ionization lead to complex, non-linear changes in observed spectral shape. In general, segments of the LOS near the accretor will pass through material that is less absorbent; the apparent column density inferred from X-ray spectroscopy is then, if a neutral absorber is assumed, smaller than the actual total column density of material and thus also than the column density computed in this paper.

A first correction can be made to the smooth wind profile (10) by accounting only for the material outside a region where the ionization parameter[2] ξ is lower than a critical value ξ_c. However, the exact value of ξ_c will depend on details of

---

[2] The ionization parameter is usually defined, after Tarter et al. (1969) as $\xi = L_x/nr^2$ with L_x the ionizing X-ray luminosity, n the number density of illuminated material and r the distance from the X-ray source. It is often expressed as $\log \xi$., with ξ in CGS units.

the observations used to obtain the absorption measurements from X-ray spectra, e.g., energy ranges considered and underlying spectral degeneracies, and on detailed (micro-)structure and composition of the wind. Only a proper radiative transfer computation can provide the insights we need on the wind ionization structure to correct the neutral column density N_H (Watanabe et al. 2006; Mauche et al. 2008). However, such simulations are not yet available for complex, dynamic clumpy winds. Interestingly, in SFXTs, the lower X-ray luminosity than in classic SgXBs should limit the impact of photoionization on the column density (Pradhan et al. 2018).

An additional problem may be posed by inhomogeneous and variable X-ray irradiation, such as when considering timescales smaller than the pulsar rotation period in HMXBs with accreting pulsars as compact object. In such systems, changes in X-ray flux can reach a factor of a few within 10–100 s, resulting in a dynamic illumination of the wind material. The resulting effects will require a dedicated investigation, also involving radiative transfer computations.

6.3. Eccentric orbits

For the sake of simplicity, we kept the number of degrees of freedom of our model limited to a minimum and discarded eccentric orbits. However, the present model can straightforwardly be extended to study a specific system where the orbit is suspected to be eccentric, especially when it comes to the fitting of the median N_H profile by the smooth wind solution (10). Although classic SgXBs such as Vela X-1 are largely circularized, SFXTs exhibit more eccentric orbits and would benefit from such an extension. For instance, the N_H profile obtained by García et al. (2018) in the SFXT IGR J16320-4751 displays a very sharp increase which the authors interpret as due to a grazing orbit. In addition, the flat N_H profile they measure away from this spike can only be reproduced either with a low inclination, incompatible with a grazing orbit, or with an eccentric orbit. They derived an eccentricity of 0.2, possibly indicative of the conditions of formation of the compact companion (Brandt & Podsiadlowski 1995). Even if they are more rare, eccentric orbits can occur in classic SgXBs too: in 2S0114+650 discussed in Section 5.1.1, some authors found an eccentricity close to 0.17 (Crampton et al. 1985; Grundstrom et al. 2007) although Koenigsberger et al. (2006) argued in favor of a zero eccentricity, which could account for the super-orbital period measured in this system.

6.4. Varying clump properties

A final limitation to be acknowledged is the unique clump mass and radius at $r = 2$ we consider. In reality, numerical simulations indicate various masses and radii for the clumps (Sundqvist et al. 2018). Ducci et al. (2009) considered the impact of a distribution of sizes and masses of the clumps to study the time variability of the mass accretion rate. We avoided introducing new parameters in the present study but such a distribution could be included in our simulations to seed the clumps. Similarly, it would be possible to study in more detail the impact of non-spherical clumps on the column density (Oskinova et al. 2012).

7. Summary

Motivated by the pressing need for a better understanding of stellar outflows from hot stars, we attempted to bridge the gap between theory and observations of winds from massive stars.

We designed a model both complex enough to fairly account for results derived by numerical simulations of line-driven winds and simple enough to be of some use to interpret the observational data from HMXBs. We highlighted how the wind microstructure could be constrained based on the variability of the column density. We provided a standard procedure to determine the radius R_{cl} and mass m_{cl} of the overdense clumps formed in the wind of the massive donor star. In practical terms, it will likely requires multiple X-ray exposures of a few $10\,\text{ks}$ each of HMXBs with moderate luminosities and orbital inclinations, around orbital phases $\phi = 0.25$ and at inferior conjunction ($\phi = 0.5$) with sensitive X-ray instruments.

We identified the fundamental parameters of the problem and showed that the standard deviation δN_H of the column density could be computed analytically based on the porosity length (Owocki & Cohen 2006), characterized here as the ratio between the clump column mass and the wind mean density. The analytical prediction is in agreement within a few percent with the measured values in the simulations based on the model we designed. The standard deviation, δN_H, was found to be a good measure of the ratio $\sqrt{m_{cl}}/R_{cl}$. We also found that the coherence time scale of N_H time series was an excellent tracer of the clump self-crossing time at the point on the LOS the closest from the donor star, provided the relative speed between the clumps and the orbiting X-ray point source was accounted for. The coherence time scale is independent of the number of clumps per unit volume, which enables us to estimate the clump radius. Using the standard deviation δN_H, we can subsequently obtain an estimate on the mass of individual clumps without resorting on arguments using the time variability of the intrinsic X-ray emission.

The heuristic model we designed is aimed at systems where the column density is essentially due to unaccreted clumps passing by the LOS, but it falls short of explaining several observations in HMXBs. Noticeably, the amount of mass accreted during X-ray flares is $10^{19-23}\,\text{g}$, orders of magnitude larger than the individual clump mass obtained by radiative hydrodynamics simulations of the line-deshadowing instability. Also, the clump sizes deduced from the duration of enhanced absorption episodes are a few times larger than expected from first principles computations. This tension between observation and theory deserves to be addressed with additional investigations of the column density in HMXBs where the intermediate to low orbital inclination guarantees that the variability of N_H is likely due to the clumps and not to large scale structures produced in the orbital plane by tidal forces.

With the advent of a new generation of X-ray satellites in the decade to come, time-resolved X-ray high resolution spectroscopy will grant us access to exquisite data. Valuable information on the morphology of the stellar wind in HMXBs, both at small and large scales, will be within our scope. Other domains will benefit from the upcoming modernization of the observing fleet. In the Active Galactic Nuclei community, several models of parametrized small scale obscurers have been designed to interpret the X-ray observations (Siebenmorgen et al. 2015; Hönig & Kishimoto 2017; Buchner et al. 2019). The origin of these structures remains largely unknown though, contrary to their clump counterparts in the wind of massive stars where they naturally form due to the line-deshadowing instabiltiy. Combined efforts to understand the propagation of X-rays in these multiphase environments will shed unprecedented light upon the structures surrounding accreting compact objects but also on the accretion process itself, strongly influenced by the ambient medium.

References

Blondin, J. M., Kallman, T. R., Fryxell, B. A., & Taam, R. E. 1990, Astrophys. J., 356, 591

Boroson, B., Vrtilek, S., Kallman, T., & Corcoran, M. 2003, Astrophys. J., 592, 516

Bozzo, E., Bernardini, F., Ferrigno, C., et al. 2017, Astron. Astrophys., 608, 1

Bozzo, E., Bernardini, F., Ferrigno, C., et al. 2017, A&A, 608, A128

Bozzo, E., Falanga, M., & Stella, L. 2008, Astrophys. J., 683, 1031

Bozzo, E., Oskinova, L., Lobel, A., & Hamann, W. R. 2017, Astron. Astrophys. Vol. 606, id.L10, 4 pp., 10, 4

Brandt, N. & Podsiadlowski, P. 1995, Mon. Not. R. Astron. Soc., 274, 461

Buchner, J., Brightman, M., Nandra, K., Nikutta, R., & Bauer, F. E. 2019, Astron. Astrophys., 629

Castor, J. I., Abbott, D. C., & Klein, R. I. 1975, Astrophys. J., 195, 157

Čechura, J., Vrtilek, S. D., & Hadrava, P. 2015, Mon. Not. R. Astron. Soc., 450, 2410

Cohen, D. H., Gagné, M., Leutenegger, M. A., et al. 2011, Mon. Not. R. Astron. Soc., 415, 3354

Cohen, D. H., Li, Z., Gayley, K. G., et al. 2014, Mon. Not. R. Astron. Soc., 444, 3729

Crampton, D., Hutchings, J. B., & Cowley, A. P. 1985, Astrophys. J., 299, 839

Driessen, F. A., Sundqvist, J. O., & Kee, N. D. 2019, Astron. Astrophys., 631, A172

Ducci, L., Sidoli, L., Mereghetti, S., Paizis, A., & Romano, P. 2009, Mon. Not. R. Astron. Soc., 398, 2152

Ducci, L., Sidoli, L., & Paizis, A. 2010, Mon. Not. R. Astron. Soc., 408, 1540

El Mellah, I. & Casse, F. 2017, Mon. Not. R. Astron. Soc., 467, 2585

El Mellah, I., Sander, A. A., Sundqvist, J. O., & Keppens, R. 2019a, Proc. Int. Astron. Union, 34

El Mellah, I., Sander, A. A. C., Sundqvist, J. O., & Keppens, R. 2019b, Astron. Astrophys., 622, A189

El Mellah, I., Sundqvist, J. O., & Keppens, R. 2018, Mon. Not. R. Astron. Soc., 475, 3240

Falanga, M., Bozzo, E., Lutovinov, A., et al. 2015, Astron. Astrophys., 577, A130

Farrell, S. A., Sood, R. K., O'Neill, P. M., & Dieters, S. 2008, Mon. Not. R. Astron. Soc., 389, 608

Feldmeier, A. 1995, Astron. Astrophys., 299, 523

Feldmeier, A., Oskinova, L., & Hamann, W. R. 2003, A&A, 403, 217

Fullerton, A. W., Massa, D. L., & Prinja, R. K. 2006, ApJ, 637, 1025

Fürst, F., Pottschmidt, K., Wilms, J., et al. 2014, ApJ, 780, 133

García, F., Fogantini, F. A., Chaty, S., & Combi, J. A. 2018, Astron. Astrophys., 618

Giménez-García, A., Shenar, T., Torrejón, J. M., et al. 2016, A&A, 591, A26

Gimenez-Garcia, A., Shenar, T., Torrejon, J. M., et al. 2016, Astron. Astrophys., 591, 25

Grebenev, S. A. & Sunyaev, R. A. 2007, Astron. Lett., 33, 149

Grinberg, V., Hell, N., El Mellah, I., et al. 2017, Astron. Astrophys., 608, A143

Grinberg, V., Leutenegger, M. A., Hell, N., et al. 2015, Astron. Astrophys., 576, A117

Grundstrom, E. D., Blair, J. L., Gies, D. R., et al. 2007, Astrophys. J., 656, 431

Haberl, F., White, N. E., & Kallman, T. R. 1989, Astrophys. J., 343, 409

Hainich, R., Oskinova, L. M., Torrejón, J. M., et al. 2020, Astron. Astrophys., 634, A49

Hamann, W.-R., Feldmeier, A., & Oskinova, L. M., eds. 2008, Clumping in hot-star winds

Hatchett, S. & McCray, R. 1977, Astrophys. J., 211, 552

Herrero, A., Kudritzki, R., Gabler, R., & Vilchez, J. 1995, Astron. Astrophys., 297, 556

Hirsch, M., Hell, N., Grinberg, V., et al. 2019, Astron. Astrophys., 626, A64

Ho, C. & Arons, J. 1987, Astrophys. J., 321, 404

Hönig, S. F. & Kishimoto, M. 2017, Astrophys. J., 838, L20

Illarionov, A. F. & Sunyaev, R. A. 1975, Astron. Astrophys., 39

In't Zand, J. J. 2005, Astron. Astrophys., 441, 2002

in't Zand, J. J. M., Bozzo, E., Qu, J., et al. 2019, Science China Physics, Mechanics, and Astronomy, 62, 29506

Joss, P. C. & Rappaport, S. A. 1984, Annu. Rev. Astron. Astrophys., 22, 537

Karino, S., Nakamura, K., & Taani, A. 2019, Publ. Astron. Soc. Japan, 71, 58

Koenigsberger, G., Canalizo, G., Arrieta, A., Richer, M. G., & Georgiev, L. 2003, Rev. Mex. Astron. y Astrofis., 39, 17

Koenigsberger, G., Georgiev, L., Moreno, E., et al. 2006, Astron. Astrophys., 458, 513

Leutenegger, M. A., Cohen, D. H., Sundqvist, J. O., & Owocki, S. P. 2013, Astrophys. Journal, Vol. 770, Issue 1, Artic. id. 80, 17 pp. (2013)., 770 [arXiv:1305.5595]

Liao, Z., Liu, J., Zheng, X., & Gou, L. 2020, Mon. Not. R. Astron. Soc., 5922

Lucy, L. B. & Solomon, P. M. 1970, Astrophys. J., 159, 879

Manousakis, A. & Walter, R. 2015, Astron. Astrophys., 58, A58

Martínez-Núñez, S., Kretschmar, P., Bozzo, E., et al. 2017, Space Sci. Rev., 212, 59

Martínez-Núñez, S., Torrejón, J. M., Kühnel, M., et al. 2014, Astron. Astrophys., 563, A70

Mauche, C. W., Liedahl, D. A., Akiyama, S., & Plewa, T. 2008, in American Institute of Physics Conference Series, Vol. 1054, American Institute of Physics Conference Series, ed. M. Axelsson, 3–11

Miškovičová, I., Hell, N., Hanke, M., et al. 2016, Astron. Astrophys., 590, A114

Najarro, F., Hanson, M. M., & Puls, J. 2011, Astron. Astrophys., 535

Nandra, K., Barret, D., Barcons, X., et al. 2013, ArXiv e-prints [arXiv:1306.2307]

Nowak, M. A., Hanke, M., Trowbridge, S. N., et al. 2011, ApJ, 728, 13

Odaka, H., Khangulyan, D., Tanaka, Y. T., et al. 2013, ApJ, 767, 70

Orosz, J. A., McClintock, J. E., Aufdenberg, J. P., et al. 2011, Astrophys. J., 742, 84

Oskinova, L. M., Feldmeier, A., & Kretschmar, P. 2012, Mon. Not. R. Astron. Soc. Vol. 421, Issue 4, pp. 2820-2831., 421, 2820

Owocki, S. P., Castor, J. I., & Rybicki, G. B. 1988, Astrophys. J., 335, 914

Owocki, S. P. & Cohen, D. H. 2001, ApJ, 559, 1108

Owocki, S. P. & Cohen, D. H. 2006, Astrophys. J., 648, 565

Owocki, S. P. & Rybicki, G. B. 1984, Astrophys. J., 284, 337

Owocki, S. P. & Sundqvist, J. O. 2018, Mon. Not. R. Astron. Soc., 475, 814

Parfrey, K. & Tchekhovskoy, A. 2017, Astrophys. J. Lett., 851, L34

Pradhan, P., Bozzo, E., & Paul, B. 2018, Astron. Astrophys., 610

Pradhan, P., Paul, B., Paul, B. C., Bozzo, E., & Belloni, T. M. 2015, Mon. Not. R. Astron. Soc., 454, 4467

Puls, J., Markova, N., Scuderi, S., et al. 2006, Astron. Astrophys., 454, 625

Puls, J., Sundqvist, J. O., & Markova, N. 2015, in IAU Symposium, Vol. 307, IAU Symposium, ed. G. Meynet, C. Georgy, J. Groh, & P. Stee, 25–36

Puls, J., Vink, J. S., & Najarro, F. 2008, Astron. Astrophys. Rev., 16, 209

Rahoui, F., Lee, J. C., Heinz, S., et al. 2011, Astrophys. J., 736

Reig, P., Chakrabarty, D., Coe, M. J., et al. 1996, Astron. Astrophys.

Sako, M., Liedahl, D. A., Kahn, S. M., & Paerels, F. 1999, Astrophys. Journal, Vol. 525, Issue 2, pp. 921-934., 525, 921

Sander, A. A., Hamann, W. R., Todt, H., Hainich, R., & Shenar, T. 2017a, Astron. Astrophys., 603

Sander, A. A. C., Fürst, F., Kretschmar, P., et al. 2017b, Astron. Astrophys. Vol. 610, id.A60, 19 pp., 610, A60

Sanjurjo-Ferrín, G., Torrejón, J. M., Postnov, K., et al. 2017, Astron. Astrophys., 606, 1

Shakura, N. I., Postnov, K. A., Kochetkova, A. Y., & Hjalmarsdotter, L. 2013, Physics-Uspekhi, 56, 321

Siebenmorgen, R., Heymann, F., & Efstathiou, A. 2015, Astron. Astrophys., 583

Sobolev, V. V. 1960, Harvard Univ. Press

Sundqvist, J. O. & Owocki, S. P. 2013, MNRAS, 428, 1837

Sundqvist, J. O., Owocki, S. P., Cohen, D. H., Leutenegger, M. A., & Townsend, R. H. D. 2012, Mon. Not. R. Astron. Soc., 420, 1553

Sundqvist, J. O., Owocki, S. P., & Puls, J. 2012, in Astronomical Society of the Pacific Conference Series, Vol. 465, Proceedings of a Scientific Meeting in Honor of Anthony F. J. Moffat, ed. L. Drissen, C. Rubert, N. St-Louis, & A. F. J. Moffat, 119

Sundqvist, J. O., Owocki, S. P., & Puls, J. 2018, Astron. Astrophys., 611

Sundqvist, J. O. & Puls, J. 2018, A&A, 619, A59

Tarter, C. B., Tucker, W. H., & Salpeter, E. E. 1969, ApJ, 156, 943

Torrejón, J. M., Schulz, N. S., Nowak, M. A., et al. 2015, Astrophys. J., 810, 102

van Kerkwijk, M. H., van Paradijs, J., Zuiderwijk, E. J., et al. 1995, Astron. Astrophys.

van Loon, J. T., Kaper, L., & Hammerschlag-Hensberge, G. 2001, Astron. Astrophys., 375, 498

Walter, R., Lutovinov, A. A., Bozzo, E., & Tsygankov, S. S. 2015, Astron. Astrophys. Rev., 23, 2

Walter, R. & Zurita-Heras, J. 2007, Astron. Astrophys., 476, 8

Watanabe, S., Sako, M., Ishida, M., et al. 2006, Astrophys. J., 651, 421

XRISM Science Team. 2020, arXiv e-prints, arXiv:2003.04962